MINISTRY OF EDUCATION AND TRAINING

VIETNAM ACADEMY OF SCIENCE OF TECHNOLOGY

GRADUATE UNIVERSITY OF SCIENCE AND TECHNOLOGY

Bui Thi Thu Hoai

FINITE ELEMENT MODELS IN GEOMETRICALLY NONLINEAR ANALYSIS OF FGM AND CNTRC BEAMS

SUMMARY OF DISSERATION ON ENGINEERING MECHANICS

Major: Engineering Mechanics

Code number: 9 52 01 01

Hanoi – 2024

The dissertation is completed at: Graduate University of Science and Technology, Vietnam Academy Science and Technology

Supervisors:

1. Supervisor 1: Prof. Dr. Nguyen Dinh Kien
2. Supervisor 2: Assoc. Prof. Dr. Tran Thi Thu Huong

Referee 1: Prof. Dr. Tran Van Lien

Referee 2: Assoc. Prof. Dr. Phan Bui Khoi

Referee 3: Assoc. Prof. Dr. Le Kha Hoa

The dissertation is examined by Examination Board of the Graduate University of Science and Technology, Vietnam Academy of Science and Technology at…… (time, date……)

The dissertation can be found at:

1. Graduate University of Science and Technology Library
2. National Library of Vietnam

PREFACE

1. The necessities of the thesis

With the development of science and technology, and new materials with higher mechanical strength, structures can be design to undergo large displacements during operating process. Nonlinear analysis of structures with large displacements is an important topic in the field of mechanics, with practical significance, attracting the attention of many scientists all over the world.

Nonlinear analysis of structures and solid materials is related to two main problems: (1) The geometrically nonlinear problem, where the structure experiences moderate displacements or large displacements; (2) The materially nonlinear problem, where the stress in one or more regions of the structure exceeds the elastic limit (elastoplastic structure). The results of large displacement analysis of structures, especially frames, and beams made from new materials are still very limited. For this reason, the thesis focuses on studying the large displacement behavior of frame and beam structures made from two types of new materials: Functionally Graded Material (FGM) and Carbon Nanotube Reinforced Composite (CNTRC). Due to the challenges that analytical methods face in analyzing large displacements of structures, this thesis uses a numerical approach, namely the Finite Element Method (FEM), to calculate mechanical characteristics such as displacement fields and stress fields of FGM and CNTRC frame and beam structures undergoing large displacements. The influence of material distribution, the geometric configuration of the structure, as well as the internal parameters of the structure (such as slenderness, material length scale parameter) on the large displacement behavior of the aforementioned frame and beam structures will be analyzed in detail.

2. Thesis objective

The main objective of the thesis is to develop finite element formulations and computer codes for large displacement analysis of beam and frame structure made from several types of new materials. Using the developed computer code, the thesis will analyze several specific problems and evaluate the influence of certain geometric and material parameters on the nonlinear behavior of frame and beam structures made from the aforementioned new materials.

3. Contents of the thesis

The thesis contains 3 chapters, in which chapter 1 presents the overview of the research situation in the analysis of FGM and CNTRC structures, with a focus on discussing the results of nonlinear analysis. The large displacement analysis of FGM and CNTRC sandwich beams, based on the total Lagrange formulation, is presented in Chapter 2. Chapter 3 uses the co-rotational formulation to develop a nonlinear beam elements for the large displacement analysis of FGM frame and beam structures, considering the effect of the micro-scale size effect. Main conclusions of the thesis are summarized in the Conclusion section.

4. Methods of study

The thesis employs the theoretical method with in conjunction with the Finite Element Method. The fundamental equations for the structure are established based on several different beam theories, while the Finite Element Method is used to construct the discrete nonlinear equilibrium equations and calculate the mechanical characteristics of the structure.

Chapter 1. OVERVIEW

This chapter presents an overview on analysis of FGM and CNTRC structures, both oversea and in Vietnam, with a focus on the results of nonlinear analysis. The results of the analysis based on numerical methods, particularly the FEM, are discussed in detail. The review indicates that the FEM is a reasonable choice to replace traditional analytical methods in the nonlinear analysis of FGM structures in general, and the large displacement behavior of FGM frames and beams in particular. Based on this review, the thesis presents the research direction and proposes specific research items.

Chapter 2. LARGE DISPLACEMENTS OF FGM AND CNTRC SANDWICH BEAMS

2.1. Introduction

Using the total Lagrange formulation, Chapter 2 develops a nonlinear beam elements for the large displacement analysis of FGM and CNTRC sandwich beams. The beam element is formulated based on the first-order shear deformation theory with a reduced integration scheme to avoid the shear locking. The influence of material distribution and sandwich configuration on the large displacement behavior of the beams is examined in detail. In particu-

lar, the effects of material homogenization models and the agglomeration of CNTs on the large displacement behavior of the beams are studied.

2.1. Sandwich FGM beam

Figure 2.1 illustrates the model of an FGM sandwich beam (FGSW) with length L, a rectangular cross-section $(b \times h)$, in a Cartesian coordinate system (x,z). Two types of the sandwich beams, namely FGM-faces and ceramic core (type A, Figure 2.1a); FGM-core and homogeneous-faces (type B, Figure 2.1b), are considered. In the figure, the $x-$axis is chosen on the mid-plane; z_0, z_1, z_2 and z_3 are, respectively, the vertical coordinates of the bottom surface, the interfaces between the layers and the top surface.

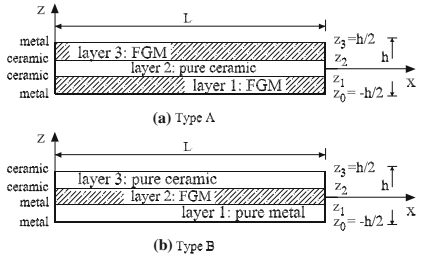

Figure 2.1. Geometry and coordinates of FGM sandwich beams.

The material properties of the sandwich beams are assumed to vary in the thickness direction in terms of constituent volume fraction by a power function. For the type A beam in Fig. 2.1a, the volume fraction of ceramic (V_c) and metal (V_m) is given by

$$V_c = \begin{cases} \left(\dfrac{z-z_0}{z_1-z_0}\right)^n, & z \in [z_0, z_1] \\ 1, & z \in [z_1, z_2] \\ \left(\dfrac{z-z_3}{z_2-z_3}\right)^n, & z \in [z_2, z_3] \end{cases} \quad \text{and} \quad V_m = 1 - V_c \tag{2.1}$$

For the type B beam in Fig. 2.1b, the volume fraction of the constituents varies in the thickness direction according to

$$V_c = \begin{cases} 0, & z \in [z_0, z_1] \\ \left(\dfrac{z-z_1}{z_2-z_1}\right)^n & z \in [z_1, z_2] \\ 1, & z \in [z_2, z_3] \end{cases} \quad \text{and} \quad V_m = 1 - V_c \tag{2.2}$$

2.3. Sandwich CNTRC beam

Fig. 2.2 shows a CNTRC sandwich cantilever with a rectangular cross-section $(b \times h)$, partially embedded on a Pasternak foundation. The beam formed from a homogeneous core and two CNTRC layers. In the figure, $x-$axis is on the mid-plane; L and L_F are the lengths of the beam and foundation supporting part; z_0, z_1, z_2 and z_3 are coordinates in the $z-$direction of the bottommost and topmost surfaces, interfaces between the layers, respectively.

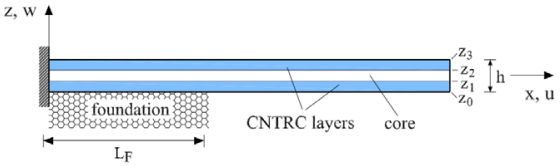

Figure 2.2. CNTRC sandwich cantilever beam partially embedded on Pasternak foundation.

Due to the low bending stiffness and high aspect ratio, CNTs tend to agglomerate in polymer matrices, creating a sort of spherical shaped inclusions, as depicted in Fig. 2.3 for a representative volume element (RVE). CNTs in the RVE are found both in bundle or clusters inside the inclusions and scattered in the matrix. This particular distribution has been described by Shi et al. [7] by a two-parameter model,which is briefly summarized below

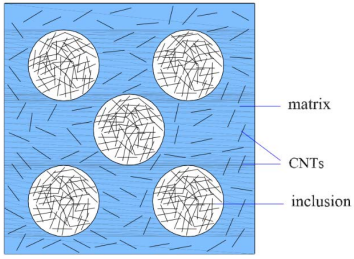

Figure 2.3. RVE with agglomerated CNT inclusions.

The total volume (V_r) of CNTs in the RVE (V) can be divided into the following two parts

$$V_r = V_r^{\text{inclusion}} + V_r^m \tag{2.3}$$

where $V_r^{\text{inclusion}}$ and V_r^m denote the volumes of CNTs dispersed in the inclusions (concentrated regions) and in the matrix, respectively.

The following parameters represent the CNT agglomeration

$$\xi = \frac{V_{\text{inclusion}}}{V}, \qquad \zeta = \frac{V_r^{\text{inclusion}}}{V_r} \qquad \text{với} \quad (\xi,\ \zeta) \in [0,\ 1] \tag{2.4}$$

In Eq. (2.4),$V_{\text{inclusion}}$ is the volume of the sphere inclusions in the RVE. ξ denotes the volume fraction of inclusions with respect to the total volume (V) of the RVE; ζ denotes the volume ratio of nanotubes that are dispersed in inclusions ($V_r^{\text{inclusion}}$) and the total volume of the nanotubes. In the case, $\xi < 1$, the agglomeration is partial with nanofillers are both in the inclusions and polymer matrix. When $\xi = 1$ nanotubes are uniformly dispersed in the matrix, and $\zeta = 1$ corresponds to the case that all the nanotubes are located in the sphere areas.

2.4. Effective properties

2.4.1 Effective properties of FGSW beam

Here, four homogenization schemes, namely the schemes due to Voigt (V), Mori–Tanaka (MT), Hashin–Shtrikman (HS) and Tamura–Tomota–Ozawa (TTO), are employed to estimate the effective elastic properties of dual-phase FGM sandwich beams.

Dual-phase FGM sandwich beams made from a ceramic and a metal are considered herein. According to the Voigt's model, an effective elastic property $(\mathscr{P}_f)$ of an FGM layer is assumed to be proportional to the volume fraction of constituent materials as [133]

$$\mathscr{P}_f(z) = \mathscr{P}_c V_c(z) + \mathscr{P}_m V_m(z) \tag{2.5}$$

where $\mathscr{P}_c$ and $\mathscr{P}_m$ denote the elastic properties of ceramic and metal.

The effective Young's modulus (E_f) and the effective Poisson's ratio (ν_f) in the Mori–Tanaka scheme [132] can be expressed as

$$E_f = \frac{9K_f G_f}{3K_f + G_f}, \quad \nu_f = \frac{3K_f - 2G_f}{6K_f + 2G_f} \tag{2.6}$$

where K_f and G_f are, respectively, the effective bulk modulus and the effective shear modulus, which can be calculated from the elastic moduli of the constituent materials

The bounds for elastic moduli of a dual-phase composite in the Hashin and Shtrikman model [134] are obtained by considering the Poisson effect of both phases. The lower bounds for effective Young's modulus (E_f), effective Poisson's ratio (ν_f) and effective shear modulus (G_f) are given by

$$E_f = \frac{9KG}{3K+G}, \qquad \nu_f = \frac{3K-2G}{2(3K+G)}, \qquad G_f = \frac{E_f}{2(1-\nu_f)} \tag{2.9}$$

The fourth scheme considered herein is due to Tamura–Tomota–Ozawa [135]. According to the TTO model, the effective Young's modulus (E_f) is

$$E_f = \frac{E_c V_c + E_m V_m \dfrac{q + E_c}{q + E_m}}{V_c + V_m \dfrac{q + E_c}{q + E_m}} \tag{2.13}$$

where q represented the ratio of stress to strain transfer.

The effective shear modulus (G_f) in the TTO model is evaluated via the Young's modulus (E_f) in Eq. (2.13) and the effective Poison's ratio (ν_f), while the effective Poison's ratio is simply calculated as $\nu_f = \nu_c V_c + \nu_m V_m$. One can verify that Eq. (2.13) deduces to the expression of the effective Young's modulus of the Voigt model in case $q = \pm\infty$.

2.4.2 Effective properties of CNTRC beam

The bulk modulus and shear modulus of the composite are obtained by Mori-Tanaka homogenization model as

$$\begin{aligned} K &= K_{\text{out}} + \left[1 + \frac{\xi \left(\dfrac{K_{\text{in}}}{K_{\text{out}}} - 1 \right)}{1 + \alpha(1-\xi) \left(\dfrac{K_{\text{in}}}{K_{\text{out}}} - 1 \right)} \right], \\ G &= G_{\text{out}} + \left[1 + \frac{\xi \left(\dfrac{G_{in}}{G_{\text{out}}} - 1 \right)}{1 + \beta(1-\xi) \left(\dfrac{G_{\text{in}}}{G_{\text{out}}} - 1 \right)} \right] \end{aligned} \tag{2.17}$$

where (K_{in}) and (G_{in}) are the effective bulk and shear moduli inside the inclusions, respectively; (K_{out}) and (G_{out}) are the effective bulk and shear moduli outside the inclusions,respectively; α and β are defines as

$$\alpha = \frac{1 + \nu_{\text{out}}}{3(1 - \nu_{\text{out}})}, \quad \beta = \frac{2(4 - 5\nu_{\text{out}})}{15(1 - \nu_{\text{out}})} \tag{2.18}$$

with $\nu_{\text{out}} = (3K_{\text{out}} - 2G_{\text{out}})/2(3K_{\text{out}} + G_{\text{out}})$. The effective Young's modulus (E) and Poisson's ratio (ν) of the composite are calculated as

$$E = \frac{9KG}{3K + G}, \quad \nu = \frac{3K - 2G}{6K + 2G} \tag{2.19}$$

2.5. Total Lagrangian beam element

2.5.1 *Vector of nodal displacements*

The vector of nodal degrees of freedom for the element, depicted in Fig. 2.4, contains six components as

$$\mathbf{d} = \{u_1 \quad w_1 \quad \theta_1 \quad u_2 \quad w_2 \quad \theta_2\}^T \tag{2.20}$$

where u_i, w_i, θ_i, $(i = 1,2)$ are, respectively, the axial, transverse displacements and rotations at node i.

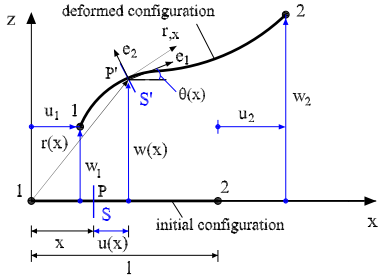

Figure 2.4. Configurations and kinematics of a two-node beam element.

The beam element with length l is initially straight and lies on the $x-$axis in a Cartesian coordinate system (x,y) as depicted in Fig. 2.4. A point P with abscissa x and its associated cross section S in the initial configuration become point P' and section S' in the deformed configuration. The deformation at the point P can be defined through an angle $\theta(x)$ - the rotation of the cross section S, and the current position vector $\mathbf{r}(x)$ of the point P' as [137]

$$\mathbf{r}(x) = [x + u(x)]\mathbf{i} + w(x)\mathbf{j} \tag{2.21}$$

where $\mathbf{i}$ and $\mathbf{j}$ are, respectively, the base unit vectors of the x and z axes; $0 \leq x \leq l$, is measured on the initial configuration; $u(x)$ and $w(x)$ are the axial and transverse displacements of the point P, respectively. The cross section S associated with point P may undergo large displacements and rotation according to the displacements $u(x)$, $w(x)$ and the rotation $\theta(x)$, as illustrated in Fig. 2.4. The vector $\mathbf{r}_{,x}(x)$ at point P', tangent to the current deformed configuration of the element, can be expressed in terms of axial and shear strains, $\varepsilon(x)$ and $\gamma(x)$, respectively, as follows

$$\mathbf{r}_{,x}(x) = \frac{d\mathbf{r}(x)}{dx} = [1 + \varepsilon(x)]\mathbf{e}_1 + \gamma(x)\mathbf{e}_2 \tag{2.22}$$

where $\mathbf{e}_1$, $\mathbf{e}_2$ are, respectively, the unit vectors, orthogonal and parallel to the current section S'. The curvature of the beam, $\kappa(x)$, at the point P is given by

$$\kappa(x) = \frac{d\theta(x)}{dx} \tag{2.24}$$

From Eqs. (2.21), one can write the axial and shear strains in the forms

$$\begin{aligned}\varepsilon(x) &= \left(1+\frac{du}{dx}\right)\cos\theta + \frac{dw}{dx}\sin\theta - 1\\ \gamma(x) &= \frac{dw}{dx}\cos\theta - \left(1+\frac{du}{dx}\right)\sin\theta\end{aligned} \tag{2.25}$$

2.5.2 Strain energy

The element strain energy U is contributed from the beam bending (U_B) and foundation deformation (U_F), $U = U_B + U_F$, in which

$$U_B = \frac{1}{2}\int_0^l \left[A_{11}\varepsilon(x)^2 + 2A_{12}\varepsilon(x)\kappa(x) + A_{22}\kappa(x)^2 + \psi A_{33}\gamma(x)^2\right]dx \tag{2.26}$$

with $\psi = 5/6$ is the shear correction factor for the beams with rectangular cross section considered herein; A_{11}, A_{12}, A_{22} and A_{33} are the rigidities of the beam.

The energy stored in the Pasternak foundation for the large deflection analysis is

$$U_F = \frac{k_W}{2}\int_0^{L_F}\left(u^2+w^2\right)dx + \frac{k_G}{2}\int_0^{L_F}(\theta-\gamma)^2 dx \tag{2.28}$$

where k_W and k_G are the Winkler and shear moduli of the Pasternak foundation; L_F is the foundation supporting length.

Interpolations are needed to introduce for the displacements and rotations. Since the displacements and rotation are independent from each another, the following linear interpolations can be employed

$$\left\{\begin{array}{c} u(x)\\ w(x)\\ \theta(x)\end{array}\right\} = \left[\begin{array}{cccccc} N_1 & N_2 & 0 & 0 & 0 & 0\\ 0 & 0 & N_1 & N_2 & 0 & 0\\ 0 & 0 & 0 & 0 & N_1 & N_2\end{array}\right]\left\{\begin{array}{cccccc} u_1 & u_2 & w_1 & w_2 & \theta_1 & \theta_2\end{array}\right\}^T \tag{2.29}$$

with

$$N_1 = \frac{l-x}{l}, \qquad N_2 = \frac{x}{l} \tag{2.30}$$

The element derived from the above linear interpolations, however suffers from the problem of shear locking [139]. To avoid this problem, the reduced integration, namely one-point Gauss quadrature, is used in this work to calculate the terms associated with shear deformation in the strain energies. In

this reagard, one can write Eqs.(2.26) and (2.28) in the following forms

$$\begin{aligned} U_B &= \frac{l}{2}\left(A_{11}\hat{\varepsilon}^2 + 2A_{12}\hat{\varepsilon}\hat{\kappa} + A_{22}\hat{\chi}^2 + \psi A_{33}\hat{\gamma}^2\right) \\ U_F &= \frac{lk_W}{6}\left(u_1^2 + u_1u_2 + u_2^2 + w_1^2 + w_1w_2 + w_2^2\right) + \frac{lk_G}{2}\left(\hat{\theta} - \hat{\gamma}\right)^2 \end{aligned} \tag{2.31}$$

where

$$\begin{aligned} \hat{\varepsilon} &= \left(1 + \frac{u_2 - u_1}{l}\right)\cos\hat{\theta} + \frac{w_2 - w_1}{l}\sin\hat{\theta} - 1 \\ \hat{\gamma} &= -\left(1 + \frac{u_2 - u_1}{l}\right)\sin\hat{\theta} + \frac{w_2 - w_1}{l}\cos\hat{\theta} \\ \hat{\chi} &= \frac{\theta_2 - \theta_1}{l} \qquad \text{với } \hat{\theta} = \frac{\theta_1 + \theta_2}{2} \end{aligned} \tag{2.32}$$

2.5.3 Vector of nodal internal forces

The element vector of nodal internal forces $\mathbf{f}_{\text{in}}$ can be split into two parts, $\mathbf{f}_{\text{in}}^B$ due to beam bending and $\mathbf{f}_{\text{in}}^F$ due to foundation deformation

$$\mathbf{f}_{\text{in}} = \mathbf{f}_{\text{in}}^B + \mathbf{f}_{\text{in}}^F \tag{2.34}$$

The above internal force vectors are computed as derivatives of the strain energies with respect to the element vector of nodal displacements as

$$\begin{aligned} \mathbf{f}_{\text{in}}^B &= \frac{\partial U_B}{\partial \mathbf{d}} = \left\{ f_{u_1}^B \quad f_{w_1}^B \quad f_{\theta_l}^B \quad f_{u_2}^B \quad f_{w_2}^B \quad f_{\theta_2}^B \right\}^T, \\ \mathbf{f}_{\text{in}}^F &= \frac{\partial U_F}{\partial \mathbf{d}} = \left\{ f_{u_1}^F \quad f_{w_1}^F \quad f_{\theta_l}^F \quad f_{u_2}^F \quad f_{w_2}^F \quad f_{\theta_2}^F \right\}^T \end{aligned} \tag{2.35}$$

2.5.4 Tangent stiffness matrix

The tangent stiffness matrix $\mathbf{k}_{\text{t}}$ of the element can also be written in the form

$$\mathbf{k}_t = \mathbf{k}_t^B + \mathbf{k}_t^F \tag{2.38}$$

where $\mathbf{k}_t^B$ and $\mathbf{k}_t^F$ are the tangent stiffness matrices stemming from the deformation of the beam and the foundation, respectively. These matrices are computed by twice differentiation of the strain energy (2.31) with respect to

the element vector of nodal displacement to

$$\mathbf{k}_t^B = \frac{\partial^2 U_B}{\partial \mathbf{d}^2} = \begin{bmatrix} k^B_{u_1u_1} & k^B_{u_1w_1} & k^B_{u_1\theta_1} & k^B_{u_1u_2} & k^B_{u_1w_2} & k^B_{u_1\theta_2} \\ & k^B_{w_1w_1} & k^B_{w_1\theta_1} & k^B_{w_1u_2} & k^B_{w_1w_2} & k^B_{w_1\theta_2} \\ & & k^B_{\theta_1\theta_1} & k^B_{\theta_1u_2} & k^B_{\theta_1w_2} & k^B_{\theta_1\theta_2} \\ & & & k^B_{u_2u_2} & k^B_{u_2w_2} & k^B_{u_2\theta_2} \\ & \text{syms.} & & & k^B_{w_2w_2} & k^B_{w_2\theta_2} \\ & & & & & k^B_{\theta_2\theta_2} \end{bmatrix} \tag{2.39}$$

and

$$\mathbf{k}_t^F = \frac{\partial^2 U_F}{\partial \mathbf{d}^2} = \begin{bmatrix} k^F_{u_1u_1} & k^F_{u_1w_1} & k^F_{u_1\theta_1} & k^F_{u_1u_2} & k^F_{u_1w_2} & k^F_{u_1\theta_2} \\ & k^F_{w_1w_1} & k^F_{w_1\theta_1} & k^F_{w_1u_2} & k^F_{w_1w_2} & k^F_{w_1\theta_2} \\ & & k^F_{\theta_1\theta_1} & k^F_{\theta_1u_2} & k^F_{\theta_1w_2} & k^F_{\theta_1\theta_2} \\ & & & k^F_{u_2u_2} & k^F_{u_2w_2} & k^F_{u_2\theta_2} \\ & \text{syms.} & & & k^F_{w_2w_2} & k^F_{w_2\theta_2} \\ & & & & & k^F_{\theta_2\theta_2} \end{bmatrix} \tag{2.40}$$

2.6. Equilibrium equation

The equilibrium equation for the large deflection analysis of the beams can be written in the following form [140]

$$\mathbf{g}(\mathbf{p},\lambda) = \mathbf{q}_{\text{in}}(\mathbf{p}) - \lambda \mathbf{f}_{\text{ef}} = \mathbf{0} \tag{2.44}$$

where the residual force vector $\mathbf{g}$ is a function of the current structural nodal displacements $\mathbf{p}$ and the load level parameter λ; $\mathbf{q}_{\text{in}}$ is the structural nodal force vector, assembled from the derived internal force vector $\mathbf{f}_{\text{in}}$, and $\mathbf{f}_{\text{ef}}$ is the fixed external loading vector. The system of equations (2.44) consists of n equations with m unknowns, which are the displacements and rotation angles at the nodes $\mathbf{p}$. The solution of the equation (2.44) corresponding to a specific value of the parameter λ gives the equilibrium points in the force-displacement space. The set of equilibrium points forms the equilibrium path.

The system of nonlinear Eq. (2.44) can be solved by an incremental/ iterative procedure based on the Newton–Raphson method.

2.7. Formulation verification

The comparison of the tip response of the FGM sandwich beam obtained herein with that of Ref. [48] is shown in Fig. 2.6 for various material grading indices and layer thickness ratios. Very good agreement between the result of the present work with that obtained by a co-rotational Euler–Bernoulli beam element of Ref. [48] can be seen from Fig. 2.6. Noting that the comparison in Fig. 2.6 is shown for the Voigt model since Ref. [48] used this model only.

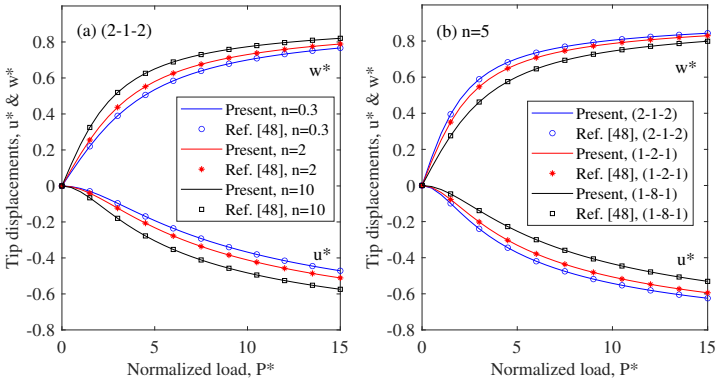

Figure 2.6. Comparison of tip response of cantilever FGM sandwich beam under a tip load.

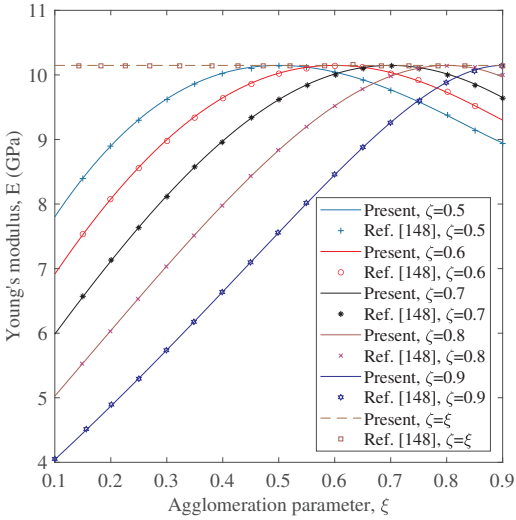

Figure 2.7. Comparison of effective Young's modulus of CNTRC with $V_{\mathrm{CNT}} = 0.1$

The effective Young's modulus of the CNTRC obtained in the present work is compared with the result of Daghigh et al. [148] in Fig. 2.7 for a

carbon nanotube volume fraction $V_{\mathrm{CNT}} = 0.1$. One can see from the figure that the present result agrees well with that of the cited reference. It can also be seen from the figure that Young's modulus considerably decreases by the CNT agglomeration, and it attains the highest value when $\xi = \zeta$, which corresponds to the fully dispersed case.

2.8. Results and discussion

2.8.1. Large displacements of FGSW beam

2.8.1.1. FGSW cantilever under a transverse load

The effects of the material distribution and homogenization scheme on the large deflection behaviour of the FGM sandwich beam can also be seen from Fig. 2.8, where the load-displacement curves and deformed configurations of the symmetric (2-1-2) type A beam are, respectively, shown for different material grading indices and homogenization schemes. Fig. 2.8a shows the above remark on the influence of the material grading index on the large displacement response of the beam. The large deflection response obtained by the MT, HS and TTO models, as seen from Fig. 2.8b is quite closed to each other, while that using the Voigt model significantly differs from the others. Among the four homogenization schemes considered herein, the Voigt model, which does not satisfy the HS bounds, is the most conservative compared to the other ones. Thus, though the Voigt model is mathematically simple, care should be taken when handling results obtained from the numerical modeling FGSW beams using this model.

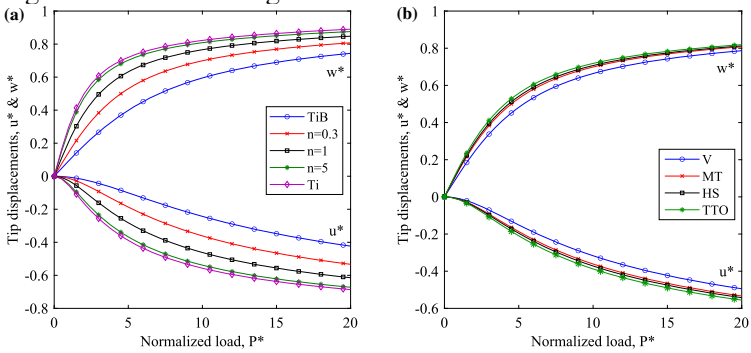

Figure 2.8. Load-displacement curves of (2-1-2) type A beam under a tip load: (a) MT model and n is variable; (b) $n = 0.3$ and different homogenization schemes.

2.8.1.2. Roll-up of FGSW cantilever

The influence of the material distribution and the homogenization scheme

on the behaviour of the beams can be seen more clearly from Fig. 2.15, where the deformed configurations of the type A and type B sandwich beams are, respectively, depicted for two values of the applied moment, $M^* = 6$ and $M^* = 10$, and different material grading indices and homogenization schemes. Fig. 2.15 clearly show the influence of the homogenization scheme on the large deflection behaviour of the beams, where the Voigt model is seen again to be the most conservative while TTO model is the most flexible. The beams curve toward circular arcs in an order as TTO, SH, MT and V models.

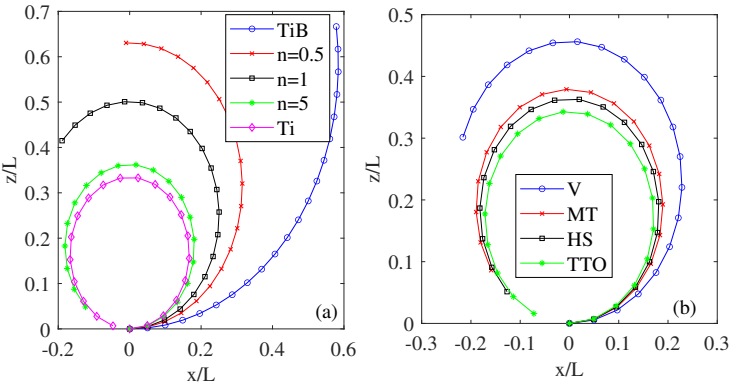

Figure 2.15. Roll-up of type A cantilever beam: (a) (2-1-2) beam with MT model, $M^* = 6$ and n is variable; (b) $n = 0.5$, $M^* = 10$ and different homogenization schemes.

2.8.1. Large displacements of CNTRC sandwich beam

The effect of CNTs agglomeration is illustrated in Fig. 2.21, where the nonlinear response of the symmetric beam (2-1-2) and the asymmetric beam (1-1-2) under transverse load at the free end of the cantilever beam with $L/h = 10$, $V_{CNT} = 0.1$, $\alpha_F = 0.4$, $\zeta = 0.9$, $(k_1, k_2) = (50, 0.5)$ and different values of agglomeration parameter ξ. As seen from Fig. 2.21, the tip response of the sandwich cantilever beam with the symmetric and non-symmetric is more pronounced when the difference between the two agglomeration parameters ξ and ζ larger. In other words, the more severe the agglomeration degree is, the larger tip displacements are, regardless of the loading type and the sandwich configuration.

Fig. 2.25 shows the load-deflection curves of the (2-1-2) symmetric and (1-1-2) non-symmetric sandwich cantilever beams under the tip load P for $L/h = 10$, $V_{CNT} = 0.1$, $\alpha_F = 0.4$, $(\xi, \zeta) = (0.4, 0.7)$ and different foun-

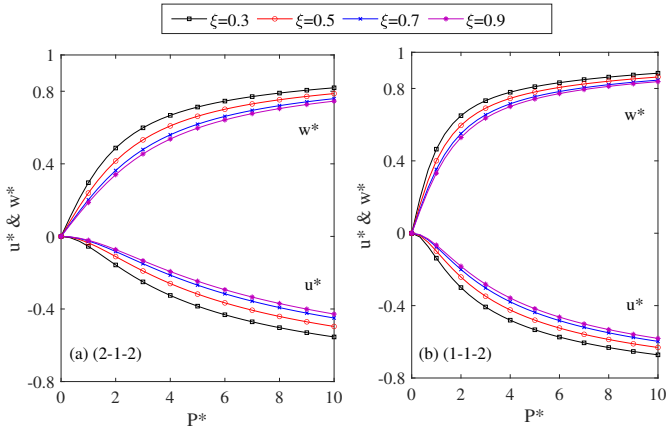

Figure 2.21. The tip response of CNTRC sandwich beam to transverse load for $(L/h = 10,$ $V_{CNT} = 0.1,\ \alpha_F = 0.4,\ \zeta = 0.9,\ (k_1, k_2) = (50, 0.5))$ and different values of ξ .

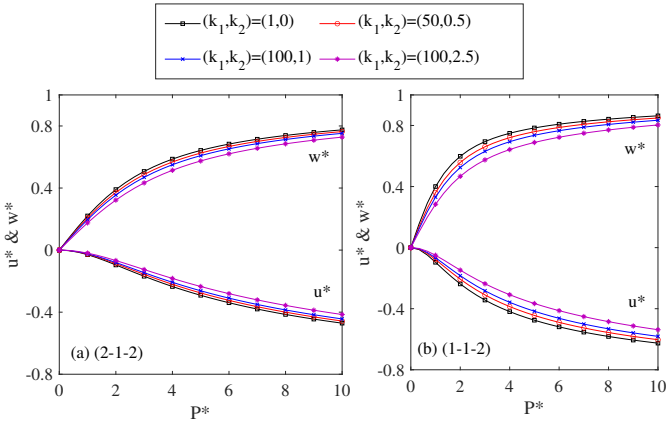

Figure 2.25. Effect of foundation stiffness on large deflections of CNTRC sandwich beams under transverse load for $(L/h = 10,\ V_{CNT} = 0.1,\ \alpha_F = 0.4,\ (\xi,\ \zeta) = (0.4, 0.7))$.

dation stiffness parameters. As expected, the tip displacements are declined by increasing the foundation stiffness, irrespective of the load level and the sandwich configuration.

Conclusions of Chapter 2

Chapter 2 develops a nonlinear beam element for studying large displacements of sandwich beams made from materials with varying mechanical properties and composite materials reinforced with carbon nanotubes. The

element is derived based on the first-order shear deformation theory and linear interpolations. The reduced integration technique is employed to avoid shear locking. The developed element in this chapter is used in conjunction with iterative algorithms and the arc-length method to develop a computational program for the nonlinear analysis of sandwich beams. Two specific problems have been analyzed and investigated in this chapter. The results of Chapter 2 have been published in the papers numbered from 1 to 7 in the "Publications related to the thesis."

Chapter 3. LARGE DISPLACEMENTS OF FGM BEAMS AND FRAMES

3.1. Introduction

The large displacement behavior of FGM beams and frames, considering the influence of micro-scale size effects, is studied in this chapter. The nonlinear beam element is developed based on the co-rotational formulation, where the element formulation is first derived in the local coordinate system and then transferred to the global coordinate system using transformation matrices. The beam element in this chapter is based on Euler-Bernoulli beam theory, incorporating the effects of micro-scale size through the Modified Couple Stress Theory (MCST). To improve the convergence of the element, polynomials derived from the solution of the nonlinear equilibrium differential equations of the element are used to interpolate the displacement field. The beam element for analyzing conventional macro-scale beams and frames is obtained from the element in this chapter by eliminating the terms related to the micro-scale size parameter. Numerical studies are conducted to illustrate the influence of material distribution and material length scale parameter on the nonlinear behavior of frame and beam structures.

3.2. FGM beam

Considering an FGM beam with rectangular cross-section $(b \times h)$. The beam is made from a mixture of ceramic and metal with the volume fraction of material constituents varying in the thickness direction according to

$$V_c = \left(\frac{z}{h} + \frac{1}{2}\right)^n, \quad V_m = 1 - V_c \tag{3.1}$$

The Voigt model and Mori-Tanaka homogenization scheme is adopted herein to estimate the effective elastic moduli of the FGM beam. According

to the Voigt model, the effective material properties $(\mathscr{P}_f)$, are evaluated by a simple rule

$$\mathscr{P}_f(z) = \mathscr{P}_c V_c(z) + \mathscr{P}_m V_m(z) \tag{3.2}$$

with $\mathscr{P}_c$, $\mathscr{P}_m$ are the material properties of ceramic and metal, respectively.

According to the Mori-Tanaka scheme [132], the effective Young's modulus (E_f) and Poisson's ratio (ν_f) are of the forms

$$E_f = \frac{9K_f G_f}{3K_f + G_f}, \quad \nu_f = \frac{3K_f - 2G_f}{6K_f + 2G_f} \tag{3.4}$$

3.3. Co-rotational framework

Fig. 3.1 shows a planar two-node beam element and its kinematics in two coordinate systems, a global system (x,z) and a local one (x_l, z_l). Based on Euler–Bernoulli beam theory, the axial displacement, $\bar{u}(\bar{x},\bar{z})$, and the transverse displacement, $\bar{w}(\bar{x},\bar{z})$, at any point of the element are given by

$$\bar{u}(\bar{x},\bar{z}) = \bar{u}_0(\bar{x}) - \bar{z}\,\bar{w}_{0,\bar{x}}(\bar{x}) \;, \quad \bar{w}(\bar{x},\bar{z}) = \bar{w}_0(\bar{x}) \tag{3.6}$$

where $\bar{u}_0(\bar{x})$ and $\bar{w}_0(\bar{x})$ are respectively the axial and transverse displacements of any point on the mid-plane; and $\bar{z}$ is the distance from the considering point to the mid-plane.

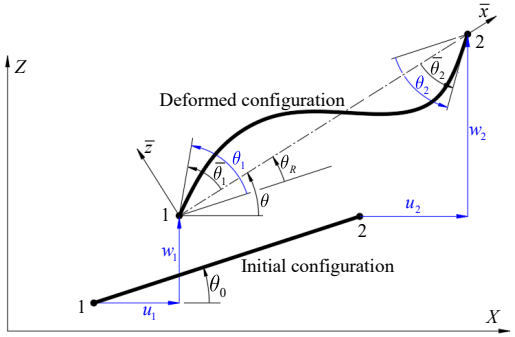

Figure 3.1. A 2-node corotational beam element and its kinematics.

The global nodal displacements in general are nonzero, and the vector of global nodal displacement, $(\mathbf{d})$, has six components as

$$\mathbf{d} = \{u_1 \quad w_1 \quad \theta_1 \quad u_2 \quad w_2 \quad \theta_2\}^T \tag{3.7}$$

where u_i, w_i and θ_i $(i = 1,2)$ are the global axial and transverse displacements and rotation at the node i respectively.

The local system (x_l, z_l) is chosen such that its original is always at the node **1**, and $x-$ axis directs towards the node **2**. With such chosen local system, the local axial displacement, x_l, at the node **1** and the local transverse displacements at both the two nodes always vanish, $\bar{u}_1 = \bar{w}_1 = \bar{w}_2 = 0$. The vector of local nodal displacements $(\bar{\mathbf{d}})$, of the element, thus contains only three components as follows

$$\bar{\mathbf{d}} = \{\bar{u} \quad \bar{\theta}_1 \quad \bar{\theta}_2\}^T, \qquad \bar{u} = u\bar{_2} \tag{3.8}$$

where $\bar{u}$ is the local axial displacements at the node 2; $\bar{\theta}_1$ and $\bar{\theta}_2$ are the local rotations at the nodes **1** and **2** respectively. In Eq. (3.8) và ở dưới đây, and hereafter, the superscript 'T' indicates the transpose of a vector or a matrix, and the bar suffix denotes a quantity with respect to the local system (x_l, z_l).

By considering the geometry of Fig. 3.1, one can obtain the relation between the local displacement and rotations with the global ones as follows

$$\bar{u} = l_n - l_o; \quad \bar{\theta}_1 = \theta_1 - \theta_r; \quad \bar{\theta}_2 = \theta_2 - \theta_r \tag{3.11}$$

with l_o and l_n are the initial and current lengths of the element, θ_r is the rigid rotation of the element.

3.4. Transformation matrix

Assuming the elastic strain energy of the element has been derived, the global nodal force vector and the global tangent stiffness matrix for the element can be obtained by successive differentiation of the strain energy with respect to the global vector of nodal displacements as follows

$$\begin{aligned} \mathbf{f}_{\text{in}} &= \frac{\partial U}{\partial \mathbf{d}} = \frac{\partial U}{\partial \bar{\mathbf{d}}} \frac{\partial \bar{\mathbf{d}}}{\partial \mathbf{d}} = \mathbf{T}_1^T \bar{\mathbf{f}}_{\text{in}}, \\ \mathbf{k}_{\text{t}} &= \frac{\partial^2 U}{\partial \mathbf{d}^2} = \mathbf{T}_1^T \bar{\mathbf{k}}_{\text{t}} \mathbf{T}_1 + \bar{N}_2 \mathbf{T}_2 + (\bar{M}_1 + \bar{M}_2)\mathbf{T}_3 \end{aligned} \tag{3.17}$$

where

$$\bar{\mathbf{f}}_{\text{in}} = \frac{\partial U}{\partial \bar{\mathbf{d}}}, \quad \text{và} \quad \bar{\mathbf{k}}_{\text{t}} = \frac{\partial^2 U}{\partial \bar{\mathbf{d}}^2} \tag{3.18}$$

are, respectively, the local nodal force vector and tangent stiffness matrix; $\mathbf{T}_1, \mathbf{T}_2, \mathbf{T}_3$ are the transformation matrices, which can be computed from Eq. (3.11)

$$\mathbf{T}_1 = \frac{\partial \bar{\mathbf{d}}}{\partial \mathbf{d}}, \quad \mathbf{T}_2 = \frac{\partial^2 \bar{u}_2}{\partial \mathbf{d}^2}, \quad \mathbf{T}_3 = -\frac{\partial^2 \theta_r}{\partial \mathbf{d}^2} \tag{3.19}$$

3.5. Strain energy

3.5.1. Euler-Bernoulli beams

The strain energy of an FGM beam element is given by

$$U = \frac{1}{2}\int_0^{l_0}\int_A \bar{\sigma}_{\bar{x}}\,\bar{\varepsilon}_{\bar{x}}\,dA\,d\bar{x}$$

$$= \frac{1}{2}\int_0^{l_0}\left[A_{11}\left(\bar{u}_{0,\bar{x}}+\frac{1}{2}\bar{w}_{0,\bar{x}}^2\right)^2 - 2A_{12}\left(\bar{u}_{0,\bar{x}}+\frac{1}{2}\bar{w}_{0,\bar{x}}^2\right)\bar{w}_{0,\bar{x}\bar{x}} + A_{22}\bar{w}_{0,\bar{x}\bar{x}}^2\right]d\bar{x} \tag{3.22}$$

where A_{11}, A_{12} and A_{22} are the beam rigidities.

3.5.3. Euler-Bernoulli micro beam

According to the MCST, the strain energy of a micro-scale beam element is given by

$$U = \frac{1}{2}\int_0^{l_0}\Big[A_{11}\left(\bar{u}_{0,\bar{x}}+\frac{1}{2}\bar{w}_{0,\bar{x}}^2\right)^2 - 2A_{12}\left(\bar{u}_{0,\bar{x}}+\frac{1}{2}\bar{w}_{0,\bar{x}}^2\right)\bar{w}_{0,\bar{x}\bar{x}} + A_{22}\bar{w}_{0,\bar{x}\bar{x}}^2 + A_{33}\bar{w}_{0,\bar{x}\bar{x}}^2\Big]dx \tag{3.38}$$

where A_{11}, A_{12}, A_{22} and A_{33} are the beam rigidities

$$(A_{11},A_{12},A_{22}) = b\int_{-h/2}^{h/2}\hat{E}_f(\bar{z})\left(1,z,z^2\right)d\bar{z}$$
$$A_{33} = bl_m^2\int_{-h/2}^{h/2}\mu_f(\bar{z})d\bar{z} \tag{3.39}$$

with the effective Young's modulus $\hat{E}_f$ defined as

$$\hat{E}_f = \begin{cases} \lambda_f + 2\mu_f & \text{with incorporating Poisson's ratio} \\ E_f & \text{without incorporating Poisson's ratio} \end{cases} \tag{3.40}$$

It should be emphasized that due to the inhomogeneity of the FG material, the axial and bending coupling rigidity A_{12} does not vanish in the microbeam model. Furthermore, because of the micro-scale size effect, the 'shear rigidity' A_{33}, which contains the material length scale parameter l_m, still appears in the expression of the elastic strain energy, even the Euler-Bernoulli beam theory is used to model the microscale frames.

3.6. Local element formulation

3.6.1. Interpolations

The interpolations for the local axial and transverse displacements in the following forms

$$\begin{aligned}
\bar{u}_0(\bar{x}) &= \frac{\bar{x}}{l_0}\bar{u}_2 + \left(\frac{3A_{12}\bar{x}^2}{A_{11}l_0^2} - \frac{3A_{12}\bar{x}}{A_{11}l_0}\right)(\bar{\theta}_1+\bar{\theta}_2) \\
&+ \left(\frac{2\bar{x}^2}{l_0} - \frac{13\bar{x}}{30} - \frac{11\bar{x}^3}{3l_0^2} + \frac{3\bar{x}^4}{l_0^3} - \frac{9\bar{x}^5}{10l_0^4}\right)\bar{\theta}_1^2 \\
&+ \left(\frac{\bar{x}^2}{l_0} - \frac{\bar{x}}{30} - \frac{11\bar{x}^3}{3l_0^2} + \frac{9\bar{x}^4}{2l_0^3} - \frac{9\bar{x}^5}{5l_0^4}\right)\bar{\theta}_1\bar{\theta}_2 \\
&+ \left(\frac{\bar{x}}{15} - \frac{2\bar{x}^3}{3l_0^2} + \frac{3\bar{x}^4}{2l_0^3} - \frac{9\bar{x}^5}{10l_0^4}\right)\bar{\theta}_2^2 \\
\bar{w}_0(\bar{x}) &= \left(\bar{x} - \frac{2\bar{x}^2}{l_0} + \frac{\bar{x}^3}{l_0^2}\right)\bar{\theta}_1 + \left(-\frac{\bar{x}^2}{l_0} + \frac{\bar{x}^3}{l_0^2}\right)\bar{\theta}_2
\end{aligned} \tag{3.44}$$

The displacements in Eq. (3.44) are used to derive the local tangent stiffness matrix and internal force vector of the beam element.

3.6.2. Internal force vector and tangent stiffness matrix

With the interpolations (3.44), one can express the strain energy of the element in Eq. (3.38) in terms of the local displacements. The local internal force vector and the tangent stiffness matrix for the element are then calculated by successively differentiating the strain energy according to Eq. (3.17).

3.7. Numerical procedure

The nonlinear equilibrium equation (2.44), Section 2.6, is still used for the analysis of large displacements of FGM frames and beams in this chapter. However, the nonlinear behavior of the frame is much more complex than that of the beam. In order to deal with the limit point, snap-through and snap-back situations, in which the structure tangent stiffness matrix ceases to be positive definite, the spherical arc-length constraint method developed is adopted herewith.

3.8. Numerical investigation

3.8.1. Macro-scale beam and frame

In Table 3.1, the normalized tip axial and transverse displacements of the Si_3Ni_4/Al cantilever obtained by different number of elements are given for a tip moment $M = 5E_mI/L$ (where E_m is Young's modulus of Al). The corresponding tip displacements computed by Eq. (3.51) are also given in the table. As seen from the table, the results using element of the present work converge very fast, and both the axial and transverse tip displacements converge to the analytical solutions by using just six elements, regardless of the index n. Since the beam element of the present work is based on the exact interpolation functions, it is capable of giving exact displacements at the nodal points [157]. It should be noted that the effect of the shift in the neutral axis position has been taken into account in both the present work and Ref. [141], and the beam under consideration having a high aspect ratio, $L/h = 50$.

Table 3.1. Convergence of the present element in determination of tip displacements of cantilever Si_3Ni_4/Al beam under a tip moment $M = 5E_mI/L$ (nELE: number of element)

Response	n	nELE				
		1	2	4	6	Eq. (3.51)
$\frac{\lvert u_0(L)\rvert}{L}$	0.3	0.3063	0.3048	0.3047	0.3047	0.3047
	1	0.5805	0.5760	0.5758	0.5757	0.5757
	5	0.9451	0.9419	0.9418	0.9417	0.9418
	10	1.0310	1.0339	1.0340	1.0340	1.0340
$\frac{w_0(L)}{L}$	0.3	0.5978	0.5990	0.5991	0.5991	0.5991
	1	0.7063	0.7139	0.7143	0.7143	0.7143
	5	0.6306	0.6670	0.6687	0.6688	0.6688
	10	0.5583	0.6106	0.6129	0.6130	0.6130

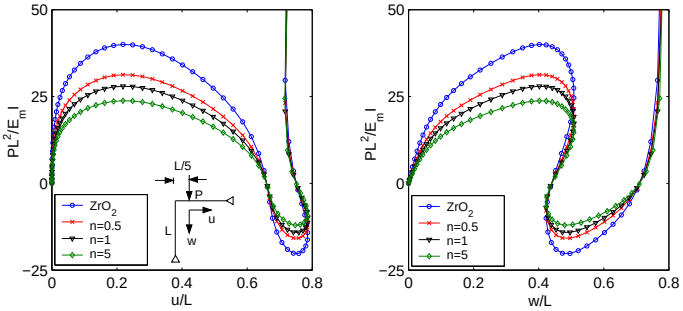

Figure 3.7. Load-displacement curves for asymmetric frame composed of ZrO_2 and Al under a point load.

The load-displacement curves of the asymmetric frame composed of Zir-

conia and Aluminum are shown in Fig. 3.7 for various values of the index n. In the figure, the axial and vertical displacements were computed at the loaded point by using ten elements, five for each beam. The influence of the material distribution on the behaviour of the frame is clearly seen from the figure, where the limit load of the frame steadily reduces when increasing the index n.

3.8.2. Micro-scale FGM beam and frame

The influence of the microstructural size parameter and Poisson's ratio can also be seen from Fig. 3.12, where the thickness distributions of the axial stress at the clamped section corresponding to $P^* = 10$ are shown for various values of the dimensionless scale parameter and two values of the powerlaw index, $n = 0.5$ và $n = 5$. One can see that the axial stress is decreased by increasing the dimensionless scale parameter and also by incorporating the Poisson's ratio, irrespective of the power-law index.

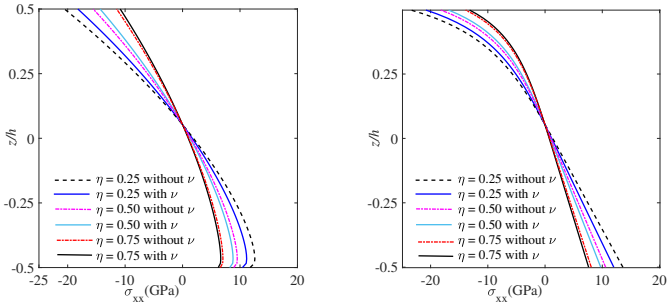

(a) $n = 0.5$ (b) $n = 5$

Figure 3.12. Thickness distribution at clamped section of axial stress of FG microcantilever corresponding to $P^* = 10$.

The deformed configurations of the microcantilever with $n = 1$ corresponding to a moment $M^* = 5.6$ as depicted in Fig. 3.14 also exhibit clearly the important role of the Poisson effect on the nonlinear bending of the microbeam. At the applied moment $M^* = 5.6$, the microcantilever associated with $\eta = 0.25$ has already rolled up to a circle for the has already rolled up to a circle for the case without Poisson's ratio effect, while it still does not when incorporating the effect of Poisson's ratio. It is worth noting that the convergence of the tip response of the microcantilever under the moment is also achieved by using five elements, but ten elements have been used in obtaining the configurations in Fig. 3.14 to ensure smoothness of the curves.

The influence of Poisson's ratio and the material length scale parameter

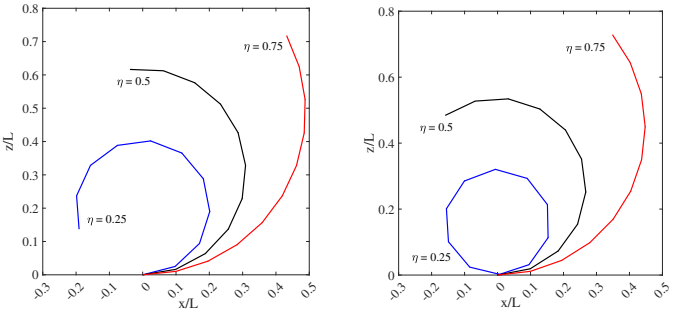

(a) With Poisson's ratio (b) Without Poisson's ratio

Figure 3.14. Deformed configurations of FG microcantilever corresponding to $M^* = 5.6$, $n = 1$ and different dimensionless scale parameters.

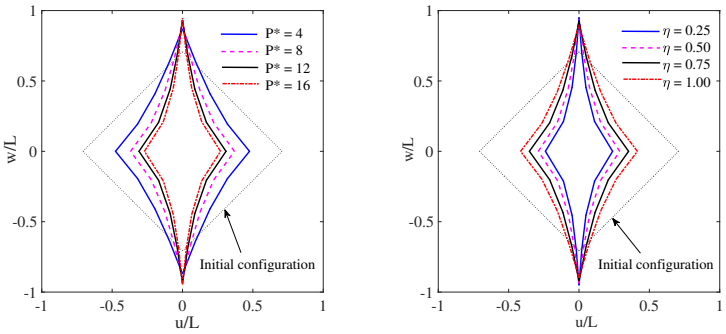

(a) $n = 0.5$, $\eta = 0.5$ (b) $n = 5$, $P^* = 10$

Figure 3.18. Deformed configurations of diamond FG microframe under tension with different values of applied load and dimensionless scale parameter ratio.

on the large displacement behavior of the micro-scale diamond FG frame can also be seen from the load-displacement curves and the deformed configurations of the frame as depicted Figs. 3.18a and 3.18b for $n = 0.5$ và $n = 5$. The micro-scale diamond frame deforms significantly when increasing the tension load (Fig. 3.18a), and it is stiffer for a larger value of the dimensionless scale parameter (Fig. 3.18b).

Conclusions of Chapter 3

Chapter 3 has developed a nonlinear beam element and numerical algorithms for the large displacement analysis of FGM frames and beams with micro-scale size effects. The beam element is constructed based on the co-rotational formulation, where Euler-Bernoulli beam theory is used in com-

bination with the MCST to describe the deformation of the beam and the size effects. To enhance the convergence of the element, polynomials derived from the solution of the nonlinear equilibrium differential equations of the element are used to interpolate the displacement field. The expressions for the tangent stiffness matrix and the internal force vector of the element are explicitly obtained. The beam element for macro-scale FGM structures is obtained as a special case of the element developed in the chapter by removing the terms that contain the micro-scale size parameter. The results of Chapter 3 have been published in papers numbered from 8 to 10 in the "Publication related to the thesis."

CONSLUSIONS

The main conclusions

• The thesis has developed two nonlinear beam elements and a computational program used for the large displacement analysis of FGM and CNTRC frames and beams. The developed beam elements and numerical program are highly effective in simulating the complex nonlinear behavior of FGM and CNTRC frame and beam structures. In particular, the beam element developed based on the co-rotational method has a simple mathematical formulation but exhibits fast convergence. Large displacements of FGM frames and beams, both with macro and micro scales, can be accurately modeled with a coarse mesh.

• The material distribution as well as practical factors such as the agglomeration of CNTs in CNTRC materials play a significant role in the nonlinear behavior of FGM and CNTRC frames and beams. The large displacement of CNTRC sandwich beams is clearly dependent on the degree of CNT agglomeration, and this agglomeration plays an important role in the nonlinear behavior of CNTRC structures. As observed in Chapter 2 of the dissertation, the agglomeration of CNTs not only makes the beam softer but also enhances the effect of shear deformation on large deflections.

• The material homogenization model used to evaluate the effective properties of composite materials plays an important role in the results obtained from the large displacement analysis of FGM sandwich beam structures. Among the four material homogenization models used in the thesis, the Voigt model is the most conservative, while the TTO model is the most flexible. Thus, though the Voigt model is mathematically simple, care should be taken

when handling results obtained numerical modeling FGSW beams using this model.

• The micro-size effect plays an important role in the nonlinear behavior of micro-sized FGM frames and beams. The large displacement of micro FGM frames and beams is significantly overestimated when ignoring the influence of the size effect. The size effect also alters the dependence of the nonlinear behavior of the frame and beam the on material parameters.

Further researches

The following problems can be considered as an extension from the thesis:

• The geometrically nonlinear behavior of micro-sized frames and beams reinforced with carbon nanotubes considers the influence of several practical factors such as the elastic foundation, temperature, and the agglomeration of carbon nanotubes.

• The materially nonlinear behavior of micro-sized FGM frames and beams is crucial. In many cases, when the structure is subjected to large loads, the stress at one or several locations of the structure exceeds the elastic limit, and therefore the influence of plastic deformation needs to be considered when studying the nonlinear bending of FGM frames and beams.

• The development of nonlinear beam elements for the analysis of three-dimensional frames and beams is a challenging task. The mathematical transformations required in deriving nonlinear beam elements for spatial frame and beam analysis are very complex and cumbersome. This demands additional time investment and requires collaboration among researchers.

PUBLICATIONS RELATED TO THE THESIS

1. Bui Thi Thu Hoai, Tran Thi Thu Huong, Nguyen Dinh Kien, Vu Thi An Ninh, Large deflection of cantilever functionally graded sandwich beam under end forces based on a total Lagrange formulation, *Vietnam Journal of Science and Technology*, 57 (6A) 2019, 32-42.
2. Bui Thi Thu Hoai, Nguyen Dinh Kien, Tran Thi Thu Huong, Le Thi Ngoc Anh, Large displacements of FGSW Beams in thermal environment using a finite element formulation, *Vietnam Journal of Mechanics, VAST*, 42(1) 2020, 43–61.
3. Bui Thi Thu Hoai, Tran Thi Thu Huong, Nguyen Dinh Kien, Large deflection of FGSW beams partially supported by a two-parameter elastic foundation using a finite element formulation, *Tạp chí Cơ khí Việt Nam*, 2020.
4. Bui Thi Thu Hoai, Nguyen Dinh Kien and Tran Thi Thu Huong, Large deflections of cantilever FG-CNTRC sandwich beams, *Hội nghị khoa học toàn quốc Cơ học vật rắn lần thứ XV*, Trường Đại học kỹ thuật công nghiệp, Đại học Thái Nguyên, 2021
5. Dinh Kien Nguyen, Thi Thu Hoai Bui, Thi Thu Huong Tran, Sergei Alexandrov, Large deflections of functionally gradedsandwich beams with influence of homogenization schemes, *Archive of Applied Mechanics*, 2022.
6. Thi Thu Hoai Bui, Thi Thom Tran, Dinh Kien Nguyen, Geometrically nonlinear analysis of sandwich composite beams reinforced by agglomeration carbon nanotubes, Vietnam Journal of Mechanics, 44(4) 2022, 376 – 391
7. Thi Thu Hoai Bui, Thi Thu Huong Tran, Vu Nam Pham, Dinh Kien Nguyen, Large deflections of agglomerated carbon nanotubes reinforced sandwich cantilever beam partially embedded on foundation, *Comptes Rendus Mécanicque*, 2024 (Accepted).
8. Thi Thu Hoai Bui, Thi Thu Huong Tran, and Dinh Kien Nguyen, Geometrically nonlinear behaviour of functionally graded beam and frame structures under mechanical loading, *RCTEMME 2021, LNME*, 326–342, 2022.
9. Thi Thu Hoai Bui, Dinh Kien Nguyen, Geometrically nonlinear behaviour of FG-CNRC sandwich beam using a co-rotational formulation, *The 7th International Conference on Engineering Mechanics and Automation (ICEMA - 2023) Hanoi,* November 11, 2023.
10. Bui Thi Thu Hoai, Le Cong Ich, Nguyen Dinh Kien, Size-dependent nonlinear bending of tapered cantilever microbeam based on modified couple stress theory, *Vietnam Journal of Science and Technology*, 62 (6) (2024) 1196-1209, doi:10.15625/2525-2518/19281.